Liver Extraction Using Residual Convolution Neural Networks From Low-Dose CT Images

Muhammad Nadeem Cheema ⓘ, Anam Nazir, Bin Sheng ⓘ, Ping Li ⓘ, Jing Qin ⓘ, and David Dagan Feng ⓘ, *Fellow, IEEE*

Abstract—An efficient and precise liver extraction from computed tomography (CT) images is a crucial step for computer-aided hepatic diseases diagnosis and treatment. Considering the possible risk to patient's health due to X-ray radiation of repetitive CT examination, low-dose CT (LDCT) is an effective solution for medical imaging. However, inhomogeneous appearances and indistinct boundaries due to additional noise and streaks artifacts in LDCT images often make it a challenging task. This study aims to extract a liver model from LDCT images for facilitating medical expert in surgical planning and post-operative assessment along with low radiation risk to the patient. Our method carried out liver extraction by employing residual convolutional neural networks (LER-CN), which is further refined by noise removal and structure preservation components. After patch-based training, our LER-CN shows a competitive performance relative to state-of-the-art methods for both clinical and publicly available MICCAI Sliver07 datasets. We have proposed training and learning algorithms for LER-CN based on back propagation gradient descent. We have evaluated our method on 150 abdominal CT scans for liver extraction. LER-CN achieves dice similarity coefficient up to 96.5±1.8%, decreased volumetric overlap error up to 4.30±0.58% , and average symmetric surface distance less than 1.4 ±0.5mm. These findings have shown that LER-CN is a favorable method for medical applications with high efficiency allowing low radiation risk to patients.

Index Terms—Computed tomography, low-dose CT, medical imaging, residual CNNs, liver extraction.

I. INTRODUCTION

COMPUTED Tomography (CT) has been a major analytical modality in the clinical field for diagnostic and pathological treatment of hepatic diseases for decades. Precise identification and marking of liver surface from CT images are vital for pre-operative analysis as well as intra-operative assessment prior to the clinical treatment [1]–[5]. Due to extensive use of medical CT, the potential cancer risk caused by overall radiation dose to a patient becomes an unsustainable aspect. Low-dose CT (LDCT) is a preferred solution to minimize radiation harms to patients [6]–[8]. However, it suffers significantly from the supplementary noise and streak artifacts. In addition, manual annotation of liver boundary grounded on a noisy pre-operative image (i.e. LDCT) is tedious, error-prone and time consuming which enforces surgeons to operate on vague estimation leads to greater mental workload and inappropriate post-operative results. Seeking a generic method that can extract soft body parts from LDCT is therefore highly demanding.

Efficient and accurate extraction of liver [9] from LDCT images is a crucial requirement yet promising challenge for effective planning in the pre-operative analysis. However, two main issues, LDCT image characteristics and diverse anatomy of soft body parts make the extraction process challenging. To counteract repetitive clinical CT examinations [10], low dose [11] strategy is becoming a critical attention of researchers. One popular way for reducing radiation dose is to shorten the exposure time of an X-ray tube. This, however, introduces strong streak artifacts [11], [12], which degrade extraction process of the organ. As a result, it could compromise the diagnostic performance and make clinical investigation difficult. To improve the image quality of LDCT, presently, many vendor-specific algorithms are proposed such as sinogram domain filtration [13] and iterative reconstruction methods [14], but they require unprocessed information with complicated data formats which are difficult to understand for most users. Due to the aforementioned constraints, the existing methods have a limited ability to denoise LDCT [15], [16] image while preserving its structural details.

Liver extraction from LDCT aims to delineate its structure and mark liver's boundary line, its accuracy is of particular importance for medical usage. Extracting organ of interest (ORI) from LDCT offers challenging issues due to countless variation

M. N. Cheema is with the Department of Computer Science and Engineering, Shanghai Jiao Tong University.

A. Nazir is with the Department of Computer Science and Engineering, Shanghai Jiao Tong University, and also with the Department of Computer Science, COMSATS University Islamabad.

B. Sheng is with the Department of Computer Science and Engineering, Shanghai Jiao Tong University, Shanghai 200240, China (e-mail: shengbin@sjtu.edu.cn).

P. Li is with the Faculty of Information Technology, Macau University of Science and Technology.

J. Qin is with the Centre for Smart Health, School of Nursing, The Hong Kong Polytechnic University.

D. D. Feng is with the Biomedical and Multimedia Information Technology Research Group, School of Information Technologies, The University of Sydney.
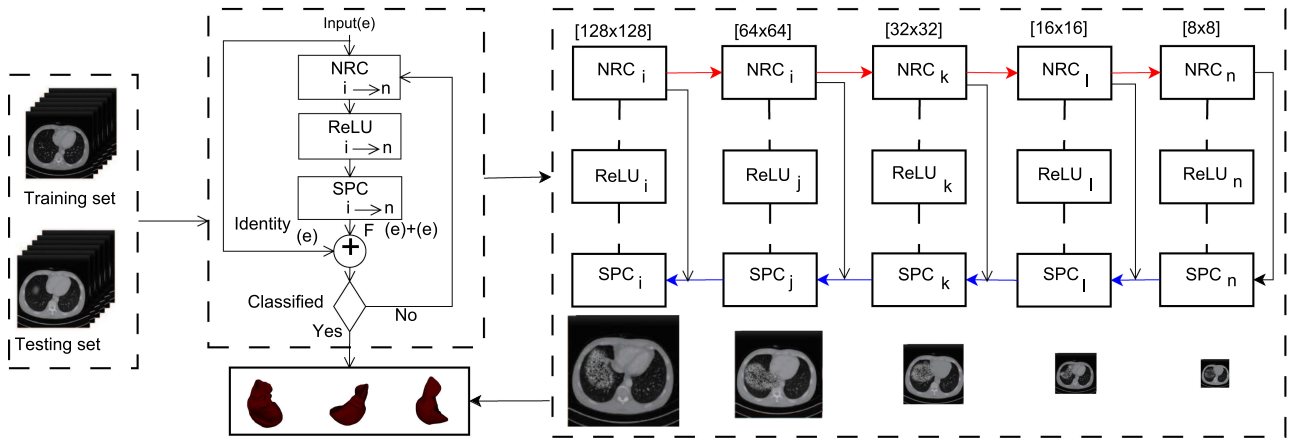
Fig. 1. Overview of the network architecture for LER-CN. First block shows the input data for training and testing LDCT image patches of size 64×64. Second block shows the component of LER-CN, i.e., five Convolution layers $NRC_{i \to n}$, five $ReLU_{i \to n}$, and five deconvolution layers of $SPC_{i \to n}$. Residual component $F(e) + (e)$ is added before final classification results and output in the form of 3D liver view points. Third block depicts detailed working of LER-CN noise removal and structural preservation components.

such as the minor difference between the liver and background structures [17], the heterogeneity of surrounding tissues [18], and huge variations in liver contour and appearance. Moreover, LDCT offers noisy data which provide poor visualization ability and restricts better analysis of pre-operative planning phase. Also, abdominal parts offer a thin band of Hounsfield (HU) ranges which restricts intensity-based methods for segmentation [19]. Several techniques such as graph cut [20], region-based [21], and thresholding have been introduced to support ORI segmentation. Thresholding is considered as traditional method for image segmentation but not designed to segment noisy image since it lacks spatial characteristics [22]. Region growing requires seed region selection in an image to be segmented. The foundation of graph cuts segments the image using an undirected weighted graph [23]. However, all the above-mentioned techniques are based on normal dose CT (NDCT). To improve the visualization problem and image quality of LDCT, Convolution Neural network (CNN) based approaches are useful alternatives in handling soft body parts extraction.

Recently, CNN-based methods are valuable research areas in medical imaging for denoising, ORI detection [24], and extraction. The patch-based CNN techniques [25] have improved segmentation by pixel-wise classification with more precise outputs. However, in spite of significant classification precision, the existing CNNs do not avoid poor results due to massive training data [26]. Although CNN shows interesting results for image segmentation, the prospective of the deep CNN has not been fully realized [15]. Most liver segmentation models based on CNN use normal dose CT modality [27], only a few are designed for extracting ORI from LDCT but are not based on CNN [28]. Aiming to minimize the potential risk of X-ray radiation to the patient, this research proposes a technique which extract liver model from denoising a LDCT image. Inspired by [15], we explore the residual CNN to address the challenging task of liver extraction from LDCT. We incorporated residual encoder-decoder CNN to denoise a low dose CT image, then extract a 3D liver model from it.

Our model referred as liver extraction residual convolution neural (LER-CN) network comprises of two basic components: Noise Removal Component (NRC) for coarse liver extraction and Structural Preservation Component (SRC) for fine liver extraction. This study differed from the work [15] by modifying their approach for extracting liver model from the LDCT image. The specific objective of this research is to reduce image noise of low-dose CT scan and extract liver 3D model using residual CNN. It will assist medical experts in pre-operative assessments such as to maximize detectability of liver lesions as well as accurate guidance during its intra-operative treatment with minimal radiation risk to patient. The key contributions of LER-CN network include:

- The LER-CN finely tunes residual convolutional neural network to mark and extract a liver model by denoising LDCT image as shown in Fig. 1.
- The liver extraction process is carried out by paired symmetric arrangement of two layers: convoluted NRC for coarse extraction and deconvoluted SPC layer for fine extraction see Fig. 2.
- We exploited the use of residual mapping to preserve spatial details of LDCT image when network goes deeper, while suppressing image noise and streak artifacts.
- The efficacy of LER-CN has validated on MICAAI Sliver07 as well as real clinical datasets. Using 3D slicer, we have extracted liver models of different view-points from LDCT see Fig. 3.

The next section describes the related work. Section III discusses the LER-CN network architecture. Experimental results obtained for our method are given in Section IV. Finally, we summarize the paper with future directions.

II. RELATED WORK

Related work for this study can be divided into following two sections i.e. image denoising approaches using CNN and liver extraction techniques based on CNN.
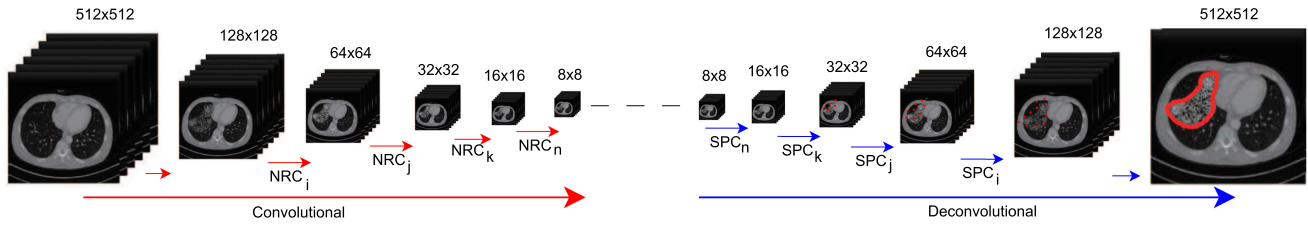
Fig. 2. Deep insight view of our two basic building blocks: symmetrical noise removal and structural preservation components. (Left) Convolution process, marked with red arrows, starts from input image [512×512×1] to remove noise from LDCT until at last layer with dimension [8×8]. (Right) Deconvolution process, marked with blue arrows, starts from image size [8×8] having five layers and ends at an extracted output image of size [512×512×1].
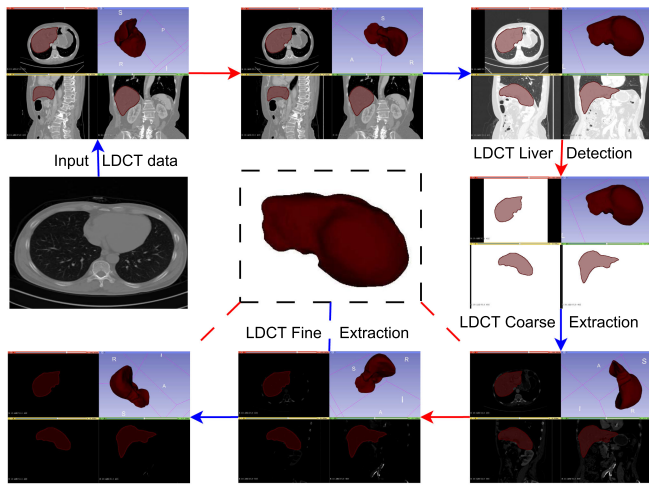

Fig. 3. Visualization of liver extraction using 3D slicer output. Coarse extractions to fine extraction, liver regions are marked red in detection phase. Different viewpoints of the liver can be seen accurately from our implemented resultant output.

A. Image Denoising Approaches Using CNN

CNNs are considered as powerful tools [29], [30] for feature extraction and classification tasks. Several methods using CNN have been proposed for denoising [31], deblurring and organ segmentation [32], [33]. To remove noise from CT image a lightweight CNN-based approach was proposed by [34]. It is also tested to denoise LDCT in "*2016 NIH-AAPM-Mayo Clinic Low Dose CT Grand Challenge*" [35]. Furthermore, techniques such as filtered back-projection (FBP) using deep CNN architecture [36] are introduced as well for LDCT to reduce reconstruction error by a factor of two. Various medical analysis tasks such as tissue segmentation, organ classification [37] and nuclei detection are accomplished using CNN models. Despite the remarkable results on CNN for LDCT, most studies are confined only to the low-level task of image denoising [15] without intention to segment and extract organ of interest from LDCT image. Although various approaches such as [38], [39] involved CNN for organ segmentation, however, the potential of CNN has not been fully realized to segment as well as to extract the desired ORI using LDCT.

B. Approaches for Liver Extraction Based on CNN

CNN is a valuable subdivision of deep artificial neural networks. Various organ segmentation approaches based on CNN

have been proposed such as lungs and brain MRIs segmentation [24], digestive system segmentation [25], and urinary bladder segmentation [27]. An end-to-end learning approach of fully connected conditional random field (CRF) [26] was proposed, by implementing fully convolutional network (FCN). Similarly, CRF refinement [40] was demonstrated in combination with FCN to improve segmentation results. Other methods have employed graph-cut approach [41] to refine FCN. These learning-based CNN techniques are dependent on predefined refinements by conventional methods for additional accuracy improvement. Furthermore, multi-organ segmentation was carried out [42] using fully convolutional network to perform end-to-end learning and pixel-to-pixel dense predictions. Similarly, quite a few techniques involved 3D fully CNN for automatic liver segmentation [41], [43] in CT images. However, more research is still necessary until the ORI extraction from LDCT images can be considered largely solved. The main limitation in traditional CNN methods is the usage of huge input data and lack of capability to finely extract ORI from LDCT images. Although state-of-the-art CNN have not trained dedicatedly for LDCT images, their potential performance undeniably motivates us to use CNN branch and explore more valuable models for medical applications.

III. METHOD

In this section, we explain our proposed LER-CN network, which takes a low dose image with streak artifacts of size [$512 \times 512 \times 1$] as input, and outputs a denoised classified image of size [$512 \times 512 \times 1$] with precise detection of ORI. The overall structural design of our LER-CN network is shown in Fig. 1. The comprehensive architecture of LER-CN consists of total 10 layers: five convolution layers consist of noise removal components and five deconvolution layers for structure preservation symmetrically arranged with their corresponding rectified linear units (ReLU), see Table I for details. The layer pattern of LER-CN network is described as $INPUT \rightarrow [[NRC \rightarrow RELU] * 5] \rightarrow [SPC \rightarrow RELU] * 5 \rightarrow OUTPUT$. Where (*) is showing the repetitions of layers. The convoluted NRC accomplishes coarse extraction by converting LDCT image to its noise free representation and delivers its output to SPC. The SPC, on the other hand, carries out fine extraction by preserving its structural details to reconstruct and compare received image with its corresponding NDCT. The noise removal and the structural preservation layers of LER-CN are structurally symmetric due to the contrary roles as shown in Fig. 2. The LER-CN pipeline consists of three key

TABLE I
DETAILED CONFIGURATION OF OUR LER-CN. NRC AND SPC DENOTE LAYERS OF NOISE REMOVAL STRUCTURAL PRESERVATION COMPONENTS, RESPECTIVELY. LETTERS NEXT TO EACH LAYER NAME SHOW THE ORDER OF CORRESPONDING LAYER IN LER-CN

Type	Kernel Size	Stride: Padding	Parameters	Depth	Output Size
input	-	-	-	-	$512{\times}512{\times}2$
NRC_i	$3{\times}3$	1:1	$27c^2$	32	$256{\times}256{\times}32$
NRC_j	$5{\times}5$	1:1	$125c^2$	64	$128{\times}128{\times}64$
NRC_k	$7{\times}7$	1:1	$243c^2$	128	$64{\times}64{\times}128$
NRC_l	$11{\times}11$	1:1	$1331c^2$	256	$32{\times}32{\times}256$
NRC_n	$13{\times}13$	1:1	$2197c^2$	512	$16{\times}16{\times}512$
$ReLU_i$	$3{\times}3$	2:0	$27c^2$	32	$256{\times}256{\times}32$
$ReLU_j$	$3{\times}3$	2:0	$125c^2$	64	$128{\times}128{\times}64$
$ReLU_k$	$3{\times}3$	2:0	$343c^2$	128	$64{\times}64{\times}128$
$ReLU_l$	$3{\times}3$	2:0	$1331c^2$	256	$32{\times}32{\times}256$
$ReLU_n$	$3{\times}3$	2:0	$2197c^2$	512	$16{\times}16{\times}512$
SPC_i	$13{\times}13$	2:1	$2197c^2$	512	$16{\times}16{\times}512$
SPC_j	$11{\times}11$	2:0	$1331c^2$	245	$32{\times}32{\times}256$
SPC_k	$7{\times}7$	1:1	$343c^2$	128	$64{\times}64{\times}128$
SPC_l	$5{\times}5$	2:0	$125c^2$	64	$128{\times}128{\times}64$
SPC_n	$3{\times}3$	1:1	$27c^2$	32	$256{\times}256{\times}32$
output	-	-	-	-	$512{\times}512{\times}2$

Algorithm 1: Training Phase of LER-CN from LDCT.

Input: I_Patches $[64 \times 64 \times 1]$, I_Parameters(K,F,S,P), Iterations

Output: $Classified\_LER - CN \leftarrow [1 \times 1 \times 2]$

  Intialize_weights←I_Parameters(K,S,F,P);

  $(NRC_i, ReLU_i, SPC_i)_{weights}$ ←inti_wei(Wd_1, He_1, Dp_1);

  for $NRC_{i \leftarrow n}$ && $ReLU_{i \leftarrow n}$ && $SPC_{i \leftarrow n}$ **do**

    Compute_outputsize $= \frac{(W_{nth} - F + 2P)}{S+1}$;

    $W_{d_2} = \frac{(W_{d_1} - F + 2P)}{S+1}$;

    $H_{e_2} = \frac{(H_{e_1} - F + 2P)}{S+1}$;

    $D_{p_2} = K$;

end for

repeat

    Move to next layer;

    Apply AND $\forall$ output sizes;

until LER-CN Unclassified

---

steps: (i) Training of LER-CN using LDCT images, (ii) Coarse extraction of liver via noise removal convolution layer, and (iii) Fine extraction of liver using structure preservation deconvolution layer see Fig. 1.

A. Training

The training process of CNN-based medical imaging applications requires an enormous amount of data samples for the sake of precise classification. This constraint is hard to meet in practice for clinical data. In our research to solve this issue, we have used the concept of fixed size overlapped patches $[64{\times}64]$ extracted from low dose and corresponding normal dose images to boost the number of training samples. For our setup, low contrast regions [44] of liver with respect to its background can be detected efficiently using above-mentioned patch-based training strategy. For first time training of LER-CN, the mapping function W is formulated by randomly initializing training $I\_parameters$ set $\sigma = K, F, S, P$ for NRC and SPC layers explained in Algorithm 1. Next, The estimation of σ is achieved by finding probabilities of output class through forward propagation by minimizing the total error $(L(c, \sigma))$ between LDCT and NDCT images denoted by Y. considering V as a set of $(y_1, z_1), (y_2, z_2), ..., (y_T, z_T)$ paired patches, total error function can be formulated as:

$$L(c, \sigma) = \frac{1}{M} \sum_{p=1}^{M} \|y_p - W(z_p)\|^2 \quad (1)$$

where y_p and z_p symbolize the normal and low dose image patches and W is the overall number of training sets. We used backpropagation to calculate the gradients of L with respect to all weights (W_p to W_T) in the LER-CN and use gradient descent to update all $I\_parameters$ values to minimize the output error

$(L(c, \sigma))$. The total error at the NRC_n layer is utilized as the loss function.

To formally define the backpropagation for our experimental setup, we have five $[M \times M]$ NRC convoluted layers with a filter λ size of $n \times n$. Our first NRC_i delivers an output of size $(M - n + 1) \times (M - n + 1)$ for calculating pre-nonlinearity input to some unit K_{vy}^m in our NRC layer, we have added up the weights with filter components for the previous layers as:

$$K_{vy}^m = \sum_{x=0}^{n-1} \sum_{z=0}^{n-1} \lambda d_{x2}^{m-1} (v + x)(y + z) \quad (2)$$

Then, our NRC applies its non-linearity as:

$$d_{vy}^m = \sigma(K_{vy}^m) \quad (3)$$

Now, to optimize all the weights and $I\_parameters$ of LER-CN to correctly classify and detect liver from LDCT training set, we apply here the chain rule to compute error for the previous NRC layers. By applying partial of E with respect to each layer's output $(\frac{\partial E}{\partial d_{vy}^m})$. Gradient component for each weight by applying chain rule is to sum the contribution of all expression in one variable as:

$$\frac{\partial E}{\partial \lambda_{xz}} = \sum_{x=0}^{M-n} \sum_{z=0}^{M-n} \frac{\partial E}{\partial K_{vy}^m} \frac{\partial k_{vy}^m}{\partial \lambda_{xz}} = \sum_{x=0}^{M-n} \sum_{z=0}^{M-n} \frac{\partial E}{\partial K_{vy}^m} d_{(v+x)(y+z)}^{m-1} \quad (4)$$

We have added up d_{vy}^m in which λ_{xz} occurs.

Compute NRC_k to NRC_n by applying chain rule as:

$$\frac{\partial E}{\partial d_{vy}^{m-1}} = \sum_{x=0}^{n-1} \sum_{z=0}^{n-1} a_1 \frac{\partial k_{(v-x)(y-z)}^m}{\partial K_{vy}^{m-1}} = \sum_{x=0}^{n-1} \sum_{z=0}^{n-1} a_1 \lambda_{xz} \quad (5)$$

The term $\frac{\partial k_{(v-x)(y-z)}^m}{\partial K_{vy}^{m-1}}$ is the value of the total error of the previous layer. Similarly, we can deduce errors for SPC layers to optimize loss function. At this stage, all the weights and $I\_parameters$ of LER-CN have now been set to correctly detect and extract liver

from LDCT testing dataset. See Algorithm 1 for the detailed training of LER-CN.

B. Coarse Extraction of the Liver Using Noise Removal Convoluted Layer

In the context of denoising LDCT, LER-CN demonstrates an excellent performance. Learning complicated features in a CNN is directly proportional to depth of the network. See Fig. 1 for our experimental setup of LDCT liver extraction process, LER-CN learn to distinguish edges and corners from low-level features in the NRC_i, then use this information to spot simple shapes in NRC_j, and next use these shapes to distinguish higher-level features, such as liver texture and its contour in advanced layers from $NRC_{k\to n}$. Unlike the traditional CNN, we use a chain of symmetrically connected noise removal convolutional layers as the stacked component. Streak artifacts in LDCT image are smoothen from low-level layer NRC_i to high-level layer NRC_n to maintain vital information in the patches. Moreover, we have abandoned the down-sampling layer to preserve important structural details. As a result, our coarse extraction phase comprises of following two layers: NRC layers and ReLU units, so the noise removal component $N_k^j(e_j)$ can be formulated as:

$$N_k^j(e_j) = ReLU(k_j * e_j + m_j) \tag{6}$$

where $j = 0, 1, \ldots, M$, M shows the number of NRC layers, K_j represents weights m_j as biases, $(*)$ operator indicates the convolution process, e_0 symbolizes patch extracted from input LDCT, and $e_j(j > 0)$ is previous layer feature. $ReLU(e) = max(0, e)$ is the formulation of an activation function. After noise removal operation, the image patches are converted to a feature space j, and the output is referred as feature vector e_m delivered to SPC layer for further operations. See Algorithm 2 for details of learning phase of the proposed method.

C. Fine Extraction of the Liver Using Structure Preservation Deconvolution Layer

Even though the down-sampling layer in LER-CN is detached, a series of NRC convolution layers still diminishes the details of an input image. We have incorporated the concept of deconvolutional into our LER-CN for preserving LDCT's structural details [38], [39]. In our fine extraction phase, the deconvolution layer reconstructs an image from the features extracted by convolution layers. We use successive deconvolutional layers named SPC to arrange the symmetrical stacked component. We use similar kernel size in the proposed method to ensure symmetry of NRC and SPC layers for generating matching input and output. We use the stack LIFO rule (Last In First Out) for data flow through the NRC and SPC layers As depicted in Fig. 1, the first NRC layer$_i$ connected to the last SPC layer$_n$, the last NRC layer$_n$ is attached to the first SPC layer$_i$ for maintaining paired symmetry. Hence, our SPC network $S_l^j(g_j)$ contains the deconvolution and ReLU layers is defined as:

$$S_l^j(g_j) = ReLU(k_j' \otimes g_j + m_j') \tag{7}$$

where $j = 0, 1, \ldots, M$, M shows the number of SPC layer, K_j represents weights, m_j indicates biases, $(\otimes)$ operator

---

Algorithm 2: Testing Phase of LER-CN from LDCT.

Input: I_Patches $[64 \times 64 \times 1]$, I_Parameters(K,F,S,P),
  Iterations from i^{th} to n^{th}
Output: $Learned\_LER - CN$
  I_Parameters←Initialize _Weights(K,S,F,P);
  LER-CN← $Prop\_Net\_Layer(I\_Patche, I\_Parameter)$;
  for $(NRC_{i=1}$ to $NRC_{i=n})$ && $(SPC_{i=1}$ to $SPC_{i=n})$
  do
    Noise_Red←Forward_Prop($I\_Parameters, ReLU_{i=n}$);
    Struct_Presv←Back_Prop($Noise\_Red_{i\to n}, ReLU_{i\to n}$);
    Total_error=$\sum \frac{1}{2}[Target\_output - desired \_output]^2$;
    Update_Weights(Loss_Fuct, Learned_LER-CN);
    repeat
    until Learned_LER-CN
  end for

---

formulate the deconvolution process, $g_m = e$ symbolizes output vector, $g_j(M > j > 0)$ is referred as previous deconvolutional layer feature vector, and g_0 is the extracted patch. After SPC operation, image patches are assembled with AND operator to extract liver area from LDCT shown in Fig. 1. Algorithm 2 is an explanation of learning process of LER-CN.

One possible implication of NRC layer is the elimination of some image details along with noise removal from LDCT [45]. Although we have incorporated SPC layer to recover some details, however, moving deeper into advanced layers of LER-CN could lead to a quite unsatisfactory loss for precise extraction of ORI. Also, with an increase in LER-CN depth, overall network training with back propagation could be difficult. To stabilize LER-CN from aforementioned two issues, we build a solution based on residual compensation method [29]. Instead of an exclusive linear flow between input and output of stacked layers, we implement a residual mapping in NRC and SPC layers [46], depicted in Fig. 1. Considering $e = input$ and $r = output$ the residual mapping is formulated as $M(e) = r - e$ and original mapping as $M(e) = R = F(e) + (e)$. Residual mapping suits our technique for two key reasons. First, it helps to optimize LER-CN training when the network is deep by evading gradient vanishing problem. Second, residual addition preserves more structural and contrast details of low dose image which can significantly enhance the precision of ORI extraction from LDCT imaging. Consequently, we have combined shortcut connection with an up-sampled output by SPC layer to achieve high resolution features for improving the object extraction process from low dose imaging.

IV. EVALUATIONS AND DISCUSSIONS

This section validates LER-CN using two datasets i.e. publicly available MICAAI Sliver07 [43] and real-time clinical dataset. The clinical data were acquired with use of automated exposure control ($150\,mAs$) and automated tube potential

selection (150 kVp). It comprises of 150 normal-dose CT volumes [512 × 512] from 50 patients including abdominal parts of the human body collected from hospital which is located in Shanghai, China. Out of total 150, 100 NDCT and corresponding LDCT image pairs were chosen for training LER-CN and the rest were used for testing purpose. The number of a voxel in our dataset were around 350 × 400 × 350, and the spacing between voxel is between (0.5mm, 0.5mm, 0.1mm) to (1mm,1mm,2mm). In preprocessing step, the volumes have been re-sampled to the spacing of (1mm,1mm,1mm), and split into slices of size 64 × 64 × 64. The simulated dataset, Sliver-07 contains 20 training and 10 testing scans [43]. LDCT images were generated for our both dataset by imposing Poisson noise [15] into the sinograms simulated from corresponding NDCT imaging with the blank scan flux of $n1 = 3 \times 10^5$ to $n3 = 3 \times 10^7$. The source and detector-to-rotation center distance was 45 and 43cm respectively. Poisson noise was inserted into the projection data for each CT image in the clinical as well as Sliver07 datasets to reach a noise level that corresponded to 30% of the normal dose.

The proposed method was implemented in C++ under the open source framework of 3D-Slicer 4.8.0 (64 bit) [47]. We used overlapping patches [64×64] with a sliding window of size 4 as the input to LER-CN. Using overlapped patches instead of whole images as an input is beneficial for LER-CN because of two reasons: First, images can be better represented by local structures and second is the requirement of huge training dataset for CNN based methods. Patching the input images can efficiently boost the training performance. LER-CN training process used standard back-propagation using stochastic gradient descent (weight decay = 0.00045, momentum = 0.12 and learning rate= 0.02 with increasing factor of 15 after five hundred iterations). The training time on clinical dataset was around 1.5 hours using a 2.70 GHz Intel Xeon E5-2680 CPU and GPU of NVIDIA GeForce GTX Titan.

A. Quantitative Evaluation

There are many factors that possibly affect the performance of LER-CN, here we focus on key aspects of radiation dose of LDCT, size of training data, and scoring systems for error metrics. For radiation dose, we select peak signal to noise ratio (PSNR), root mean square error (RMSE), and structural similarity index (SSIM) as metrics [15]. To quantitatively evaluate noise removal results for LER-CN, we have measured PSNR, RMSE, and SSIM of LDCT images in the testing set of our both public and clinical dataset with K-SVD [48] and CNN10 [35] techniques. It can be seen in Table II that, for all the metrics of Fig. 4, our proposed method achieved the best results for denoising LDCT image.
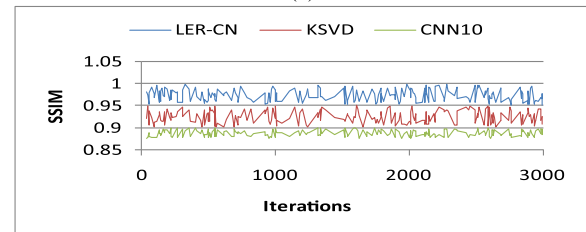
As shown in Table III segmentation accuracy measure in terms of Dice Similarity Coefficient (DSC%) and Jaccard Index (JI%) on LDCT has been improved as compared to NDCT images. The noise levels of LDCT images in the training and testing sets were constant in our technique. However, the noise level of target images was not constantly obtainable. Hence, we use varied noise levels of training and testing images to validate the strength of LER-CN as shown in Table IV. We also

TABLE II
COMPARISON OF LER-CN WITH TWO STATE-OF-THE-ART METHODS IN TERMS OF NOISE REMOVAL AND STREAK ARTIFACTS USING PEAK SIGNAL TO NOISE RATIO (PSNR), ROOT MEAN SQUARE ERROR (RMSE), AND STRUCTURAL SIMILARITY INDEX (SSIM) AS METRICS
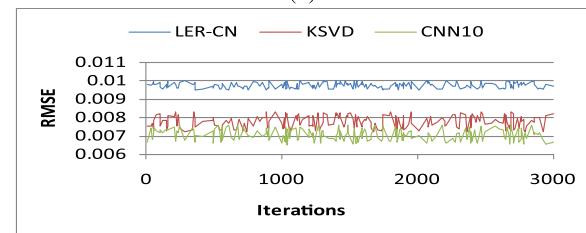
Dataset	Metrics	K-SVD	CNN10	**LER-CN**
MICCAI SLiver07 [43]	PSNR	40.6901	41.6843	**42.3841**
	RMSE	0.0182	0.0177	**0.0098**
	SSIM	0.9127	0.8921	**0.9921**
Clinical Data	PSNR	41.6901	42.6843	**43.6901**
	RMSE	0.0193	0.0184	**0.0199**
	PSNR	0.9500	0.9711	**0.9931**
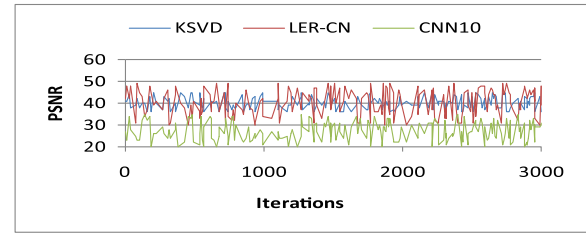
(a)

(b)

(c)

Fig. 4. Noise removal in LDCT images using NRC component values of (a) PSNR, (b) SSIM, and (c) RMSE, plotted VS number of iterations for LER-CN compared with KSVD and CNN10 methods. LER-CN shows greater efficacy in terms of all three measuring parameters.

TABLE III
SEGMENTATION ACCURACY MEASURE IN TERMS OF DICE SIMILARITY COEFFICIENT (DSC%) AND JACCARD INDEX (JI%) ON LDCT AND NDCT IMAGES WITH CLINICAL AND SLIVER07 DATASETS, WHERE DSC AND JI = 100% SHOWS PERFECT SEGMENTATION. RESULTS REVEAL THAT LER-CN HAS BEEN IMPROVED WHILE USING LOW DOSE CT IMAGES

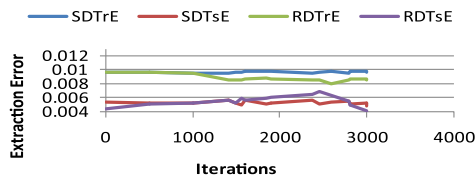| Image Type	Clinical Dataset		Sliver07 Dataset	
	DSC (%)	JI (%)	DSC (%)	JI (%)
LER-CN on NDCT	92.60±1.8	93.40±2.0	90.30±2.0	91.9±1.07
LER-CN on LDCT	**96.50±1.8**	**97.50±1.9**	**92.10±3.4**	**93.0±2.4**

TABLE IV
QUANTITATIVE MEASUREMENTS OF PIXEL ACCURACY, MEAN ACCURACY, MEAN REGION INTERSECTION OVER UNION (IU),
FREQUENCY WEIGHTED IU FOR LER-CN WITH RESPECT TO VARIABLE NOISE LEVELS

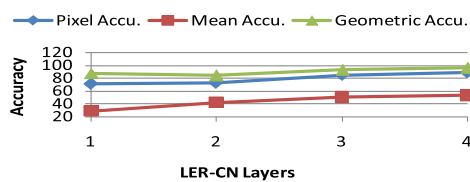| Noise Level	No. of Layers	Pixel Accuracy	Mean Accuracy	Mean IU	f.w IU	Geometric Accuracy	Inference Time
$n_1=3\times10^5$	LER-CN-L_i	76.7	30.6	29.0	71.3	89.2	$\sim$150s
	LER-CN-L_j	75.6	41.3	29.2	72.5	90.0	$\sim$150s
	LER-CN-L_k	85.2	51.7	39.5	76.1	94.3	$\sim$175ms
	LER-CN-L_n	87.3	52.1	42.0	77.4	95.5	$\sim$120ms
$n_2=3\times10^6$	LER-CN-L_i	70.8	29.3	27.2	69.3	88.1	$\sim$75s
	LER-CN-L_j	72.3	42.2	31.1	68.4	84.2	$\sim$175s
	LER-CN-L_k	85.2	50.4	38.5	75.7	93.4	$\sim$180ms
	LER-CN-L_n	88.5	53.7	41.2	78.1	96.0	$\sim$130ms
$n_3=3\times10^7$	LER-CN-L_i	71.6	29.3	30.4	70.8	86.3	$\sim$80s
	LER-CN-L_j	73.4	39.1	35.2	72.1	88.4	$\sim$90s
	LER-CN-L_k	86.5	53.5	37.8	79.0	93.1	$\sim$190ms
	LER-CN-L_n	89.2	55.0	40.5	80.1	95.6	$\sim$150ms

TABLE V
QUANTITATIVE RESULTS FOR LIVER EXTRACTION IN TERMS OF MEAN IU FOR
LOW DOSE CT (LDCT) AND CORRESPONDING NORMAL DOSE CT (NDCT)
IMAGES AGAINST LER-CN NETWORK LAYERS. THREE REGIONS OF
INTEREST (ROI1, ROI2, AND ROI3) WERE SELECTED SHOWING
MEAN IU VALUES OF LER-CN LAYERS i TO n

Image Type	Layers	Testing set			
		Mean IU		Pixel Accuracy	
		RoI_1	RoI_2	RoI_3	RoI_4
NDCT	$Layer_i$	47.9	48.9	42.5	43.4
	$Layer_j$	43.4	32.4	35.2	45.2
	$Layer_k$	41.4	39.4	36.7	39.2
	$Layer_n$	50.5	51.5	46.1	47.6
LDCT	$Layer_i$	48.9	35.4	42.1	43.1
	$Layer_j$	44.1	36.4	47.1	48.2
	$Layer_k$	40.7	39.4	48.9	49.2
	$Layer_n$	55.0	57.0	60.1	48.3

(a)

(b)

Fig. 6. Mean IU plotted for low-dose and corresponding normal-dose images against LER-CN network layers. (a) Three regions of interest (ROI_1, ROI_2, ROI_3) were selected for visualizing mean IU for LDCT images with respect to LER-CN Layer i to n. (b) Three regions of interest (ROI_1, ROI_2, ROI_3) were selected for visualizing mean IU for corresponding NDCT images with respect to LER-CN Layer i to n.
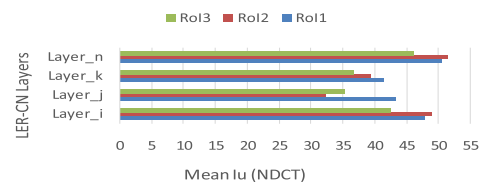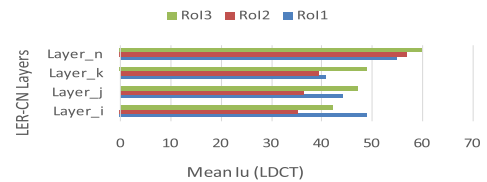

(a)

(b)

Fig. 5. Training and testing errors for coarse and fine extraction plotted for MICCAI-Sliver07 and clinical datasets with respect to number of iterations. (a) Simulated data training error (SDTrE), simulated data testing error (SDTsE), real data training error (RDTrE), and real data testing error (RDTsE). (b) Pixel Accuracy, mean accuracy, and geometric accuracy plotted against the LER-CN layers.

TABLE VI
QUANTITATIVE RESULTS ASSOCIATED WITH TRAINING AND TESTING ERRORS
FOR COARSE AND FINE EXTRACTION OF SLIVER07 AND CLINICAL DATASETS

Dataset	LER-CN	Training Error	Testing Error
MICCAI Sliver07 [43]	Coarse extra	0.00599	0.00567
	Fine extra	**0.00497**	**0.0036**
Clinical Data	Coarse extra	0.00457	0.00372
	Fine extra	**0.00487**	**0.00351**

state four metrics pixel accuracy, mean accuracy, mean region intersection over union (IU), and frequency weighted IU for LER-CN with respect to variable noise levels. Table V gives the statistical analysis and performance of our LER-CN on the test sets for the above-mentioned metrics. Also, see Fig. 5b for

graphical representation. We achieve the best results for LDCT imaging on mean IU as described in Table V and Fig. 6, by a relative margin of 15% than NDCT imaging. Also, Inference time is reduced to 120s from LDCT with image noise=3×10^3.

Another essential factor for evaluating the sensitivity of LER-CN is the size of training data. Fig. 5a shows the training and testing loss of our method on Sliver07 and clinical datasets. The testing loss of fine extraction on clinical dataset is inversely proportional to number of training samples, while the loss for coarse extraction was relatively high shown in Table VI. It reveals that with excessive training, the performance of our LER-CN can be

TABLE VII
COMPARISON OF LER-CN WITH STATE-OF-THE-ART ON CLINICAL DATASET: CRITERIA HAVING SCORE MEASURED IN TERMS OF SEVEN ERROR
METRICS, NAMELY, DICE SIMILARITY COEFFICIENT (DSC), JACCARD INDEX (JI), VOLUMETRIC OVERLAP ERROR (VOE), RELATIVE
VOLUME DIFFERENCE (RVD), AVERAGE SYMMETRIC SURFACE DISTANCE (ASD), MAXIMUM SYMMETRIC SURFACE
DISTANCE (MSD), AND ROOT MEAN SQUARE SYMMETRIC SURFACE DISTANCE (RMSD)

Methods	Score	VOE (%)	RVD (%)	ASD (mm)	RMSD (mm)	MSD (mm)	DSC (%)	JI (%)	Time (min)
Hu et al. [42]	81.6±1.3	5.20±1.2	0.38±4.5	1.3±0.5	1.23±0.27	14.01±3.30	94.3±1.9	-	15
Gauriau et al. [50]	80.4±4.0	6.34±0.71	1.03±2.8	10.6±1.2	1.62±0.30	13.59±4.31	74.9±4.0	93.4±2.8	7-8
Linguraru et al. [51]	82.5±3.1	5.64±2.3	1.84±6.3	1.1±0.7	1.79±0.95	15.82±2.32	95.2±1.2	-	7
Tong et al. [52]	77.3±4.0	5.69±0.44	-0.04±4.4	5.8±1.3	1.97±0.90	16.69±8.02	94.9±1.2	90.1±3.0	-
Okada et al. [53]	76.5±2.3	6.07±0.92	1.04±2.8	1.7±0.6	1.61±0.99	18.32±4.31	95.1±8.1	85.9±10.7	40.2
Wolz et al. [54]	84.2±1.2	4.32±2.8	0.96±1.3	1.2±0.9	1.24±0.51	17.69±3.87	94.01±9.2	89.1±4.3	7-9
He et al. [55]	83.2±1.9	6.41±2.1	1.08±20.4	1.3±0.7	-	16.74±3.23	93.3±0.9	85.4±9.7	10-15
LER-CN	**84.8±1.2**	**4.30±0.58**	**1.28±0.19**	**1.4±0.5**	**1.10±0.26**	**17.88±3.61**	**96.5±1.8**	**92.1±3.4**	**5-6**

improved by many folds. Quantitative evaluation of LER-CN is carried out using a scoring system inspired by [49]. The score for LER-CN is defined as:

$$\pi_i = max\left(100 - 25^* \frac{\alpha_i}{\overline{\alpha_i}}, 0\right) \quad (8)$$

$$\pi = \frac{1}{M}\sum_{i=1}^{M}\pi_i \quad (9)$$

where π represents final score when fine liver extraction is completed, π_i is the score derived for each layer $i \rightarrow n$ of LER-CN network, α_i is the real value of the resultant metric for each layer, and $\overline{\alpha_i}$ is the mean value for outputs delivered from NRC and SPC layer.

Table VII describes scoring criteria along with seven volume and surface distance-based error metrics, namely, Dice Similarity Coefficient (DSC), Jaccard Index (JI), Volumetric Overlap Error (VOE), Relative Volume Difference (RVD), Average Symmetric surface Distance (ASD), Maximum Symmetric surface Distance (MSD), and Root Mean square Symmetric surface Distance (RMSD) [42], [49]. Among these metrics, DSC and JI as 100% indicate perfect segmentation, ASD=0 mm shows an ideal match between the extracted ORI and the ground-truth of liver. VOE=0 represent faultless segmentation and 1 if both conditions do not overlie. RVD=0 means both volumes are indistinguishable. RMSD is susceptible to outliers and returns maximum error. Generally, it is tricky to compare the proposed study with state-of-the-art due to diverse datasets and different evaluation metrics. We have roughly compared our LER-CN network in Table VII with seven previously implemented segmentation methods [42], [50]–[55], based on the following metrics: VOE (%), DSC (%), JI (%), ASD (%), RVD (mm), RMSD (mm), MSD (mm), final score and computation time. The study by Linguraru et al. [51] developed a 4D graph model for multiple organ segmentation and achieved inspiring results. However, there method uses a small dataset for evaluation with high-resolution CT images. The findings of Tong et al. [52] and Wolz et al. [54] are costly due to the rigorous registration process. Although the assessment is conducted on different datasets of variable sizes, Table VII still emphasizes LER-CN advantages in terms of computational time (of around 5-6 minutes) over other methods.
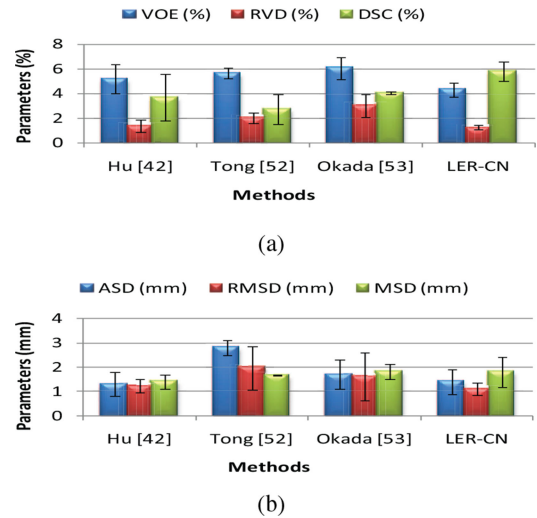
(a)

(b)

Fig. 7. Comparison of LER-CN method with state-of-the-art. (a) Box plot to represent VOE (%), RVD (%), and DSC (%), where LER-CN shows better performance comparable to other three methods. (b) Box plot to represent ASD (mm), RMSD (mm), and MSD (mm), where LER-CN shows comparable result to Hu et al. [42].

Table VII indicates that, in terms of DSC, RVD, JI, MSD and VOE, LER-CN achieved competitive performance with an increased value of DSC up to 96.5±1.8%, RVD up to 1.28±0.19%, JI= 92.5±3.4%, MSD=17.88±3.61 mm and decreased value of VOE up to 4.30±0.58%. Also, all of the above-mentioned techniques were not designed to work on low-dose CT imaging. Clearly, the proposed LER-CN can mark ORI more accurately than previous methods from LDCT with best scores relative to error metrics. Results are depicted from error graphs in Fig. 7a and Fig. 7b.

B. Qualitative Evaluation

Qualitative results from Fig. 8 show that LER-CN has suppressed noise streaks clearly from LDCT and precisely mark liver boundary to extract liver structure. Furthermore, fine extraction phase depicted in Fig. 8 indicates that utilizing SPC and residual mapping, contextual information is extracted more clearly in places where the contrast of liver area is low. Although there are still minor indistinct regions where the liver boundary is not so exact, the results of our method are more precise in
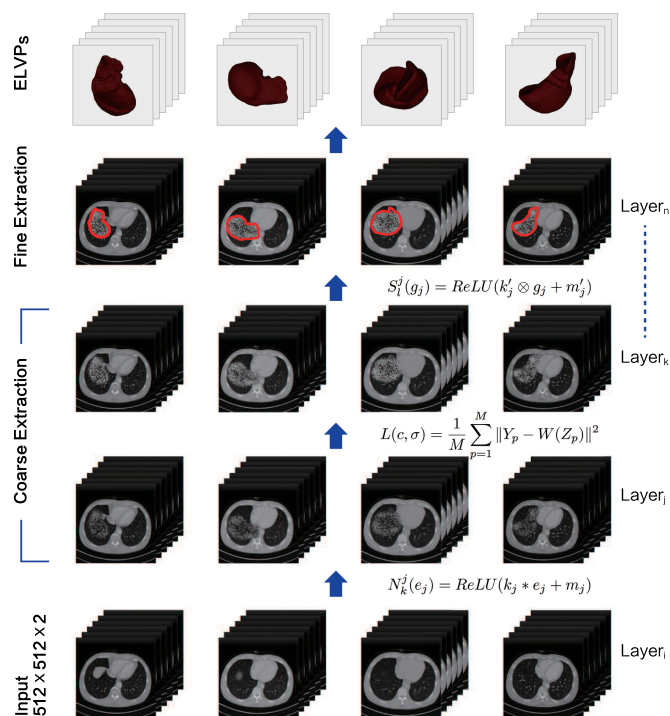
extraction task. The main strength of LER-CN network for accurate liver extraction process lies in a combination of noise removal, structure preservation, and residual mapping trained by overlapped patches. Our technique outperforms all other approaches in terms to denoise a low dose CT and as well as preserve structural details. Extending residual CNN to organ extraction and improving the architecture for LDCT images dramatically improves the state-of-the-art, while concurrently simplifying and speeding up training and learning process. Our quantitative evaluation on MICCAI Sliver07 and clinical datasets along with comparisons of state-of-the-art segmentation methods revealed that LER-CN can mark and extract liver model precisely and competently. The increased values of DSC and RVD along with lower values of VOE and ASD emphasize that LER-CN could be potentially used for hepatic diagnosis and treatment in pre-operative planning as well as intra-operative assessment. In the future, we plan to enhance LER-CN architecture for other soft body parts.

Fig. 8. Coarse and fine liver extraction. Input LDCT images of size [512×512×1], $Layer_i$ includes (NRC_i, $ReLU_i$ and SPC_i) to remove additional noise streak artifacts from LDCT, next $Layer_j$ converts liver area slightly lighter than background. Similarly, $Layer_k$ preserves structure properties of liver, black and white spots can be seen in $Layer_k$ output along with final marking of liver boundary using red colored in $Layer_n$ output images. Top layer shows 3D slicer output with extracted liver view points (ELVPs).

Equations in figure:
$$S_i^j(g_j) = ReLU(k_j' \otimes g_j + m_j')$$
$$L(c, \sigma) = \frac{1}{M} \sum_{p=1}^{M} \|Y_p - W(Z_p)\|^2$$
$$N_k^j(e_j) = ReLU(k_j * e_j + m_j)$$

comparison to those generated from state-of-the-art [42], [50]–[55]. This evidenced the efficacy of LER-CN qualitatively. Fig. 3 shows illustrative examples of liver extraction by LER-CN with a 3D-Slicer output. The two cases correspond to coarse and fine extraction results in terms of DSC. The fine extraction leads to DSCs of 96.5% for the liver, while the coarse extraction gave DSCs of 95.2% for the liver. As it can be seen from box plots of extraction process in Fig. 7, our LER-CN can predict even rough shapes for most cases in LDCT dataset. Also, the use of symmetric convolution and deconvolution layers is a reasonable ORI extraction hypothesis used in an efficient way as compared to direct mapping. The way through which the liver region from LDCT image is evaluated incorporates both lower and high-level information, and thus the impact of training loss on classification error can be alleviated as shown in (Fig. 5a). Texture preservation within the liver is another separate challenging task for our case to be solved (due to use of LDCT image) which we will hope to achieve in the future as a continuation of our proposed model.

V. CONCLUSION

We propose a liver extraction method from LDCT images to help the physician distinguish disease and plan a proper intra-operative setup with low radiation risk to a patient. We finely tuned residual convolutional neural network classifier for organ

REFERENCES

[1] N. Lessmann *et al.*, "Automatic calcium scoring in low-dose chest CT using deep neural networks with dilated convolutions," *IEEE Trans. Med. Imag.*, vol. 37, no. 2, pp. 615–625, Feb. 2018.

[2] H. Liao *et al.*, "Joint vertebrae identification and localization in spinal CT images by combining short- and long-range contextual information," *IEEE Trans. Med. Imag.*, vol. 37, no. 5, pp. 1266–1275, May 2018.

[3] G. Zhang *et al.*, "Generalized adaptive Gaussian Markov random field for X-ray luminescence computed tomography," *IEEE Trans. Biomed. Eng.*, vol. 65, no. 9, pp. 2130–2133, Sep. 2018.

[4] Y. Pei *et al.*, "Superimposition of cone-beam computed tomography images by joint embedding," *IEEE Trans. Biomed. Eng.*, vol. 64, no. 6, pp. 1218–1227, Jun. 2017.

[5] P. Lu *et al.*, "Highly accurate facial nerve segmentation refinement from CBCT/CT imaging using a super-resolution classification approach," *IEEE Trans. Biomed. Eng.*, vol. 65, no. 1, pp. 178–188, Jan. 2018.

[6] Q. Yang *et al.*, "Low dose CT image denoising using a generative adversarial network with Wasserstein distance and perceptual loss," *IEEE Trans. Med. Imag.*, vol. 37, no. 6, pp. 1348–1357, Jun. 2018.

[7] X. Zheng *et al.*, "PWLS-ULTRA: An efficient clustering and learning-based approach for low-dose 3D CT image reconstruction," *IEEE Trans. Med. Imag.*, vol. 37, no. 6, pp. 1498–1510, Jun. 2018.

[8] H. Shan *et al.*, "3D convolutional encoder-decoder network for low-dose CT via transfer learning from a 2D trained network," 2018, arXiv:1802.05656.

[9] M. N. Cheema *et al.*, "Image-aligned dynamic liver reconstruction using intra-operative field of views for minimal invasive surgery," *IEEE Trans. Biomed. Eng.*, to be published.

[10] V. Cherukuri *et al.*, "Learning based segmentation of CT brain images: Application to postoperative hydrocephalic scans," *IEEE Trans. Biomed. Eng.*, vol. 65, no. 8, pp. 1871–1884, Aug. 2018.

[11] H. Li and K. Mueller, "Low-dose CT streak artifacts removal using deep residual neural network," in *Proc. Int. Meeting Fully Three-Dimensional Image Reconstruction Radiol. Nucl. Med.*, 2017, vol. 14, pp. 191–194.

[12] K. Imai *et al.*, "Statistical characteristics of streak artifacts on CT images: Relationship between streak artifacts and mA s values," *Med. Phys.*, vol. 36, no. 2, pp. 492–499, 2009.

[13] M. Balda *et al.*, "Ray contribution masks for structure adaptive sinogram filtering," *IEEE Trans. Med. Imag.*, vol. 31, no. 6, pp. 1228–1239, Jun. 2012.

[14] A. Manduca *et al.*, "Projection space denoising with bilateral filtering and CT noise modeling for dose reduction in CT," *Med. Phys.*, vol. 36, no. 11, pp. 4911–4919, 2009.

[15] H. Chen *et al.*, "Low-dose CT with a residual encoder-decoder convolutional neural network," *IEEE Trans. Med. Imag.*, vol. 36, no. 12, pp. 2524–2535, Dec. 2017.

[16] H. Chen *et al.*, "Low-dose CT via convolutional neural network," *Biomed. Opt. Express*, vol. 8, no. 2, pp. 679–694, 2017.

[17] J. Hendrik Moltz *et al.*, "Segmentation of liver metastases in CT scans by adaptive thresholding and morphological processing," in *Proc. MICCAI Workshop*, 2008, vol. 41, pp. 1–8.

[18] K. G. Devi and R. Radhakrishnan, "Segmentation of multiple organ from abdominal CT images using 3D region growing and gradient vector flow," *Int. J. Appl. Eng. Res.*, vol. 9, no. 24, pp. 30023–30041, 2014.

[19] M. A. Selver, "Segmentation of abdominal organs from CT using a multi-level, hierarchical neural network strategy," *Comput. Methods Programs Biomed.*, vol. 113, no. 3, pp. 830–852, 2014.

[20] M. Oda *et al.*, "Organ segmentation from 3D abdominal CT images based on atlas selection and graph cut," in *Proc. MICCAI Workshop Comput. Clin. Challenges Abdominal Imag.*, 2012, pp. 181–188.

[21] J. Peng *et al.*, "3D liver segmentation using multiple region appearances and graph cuts," *Med. Phys.*, vol. 42, no. 12, pp. 6840–6852, 2015.

[22] P. I. Kalmar *et al.*, "The impact of iterative reconstruction on image quality and radiation dose in thoracic and abdominal CT," *Eur. J. Radiol.*, vol. 83, no. 8, pp. 1416–1420, 2014.

[23] S. Luo, "Review on the methods of automatic liver segmentation from abdominal images," *J. Comput. Commun.*, vol. 2, no. 2, pp. 1–7, 2014.

[24] B. Kayalibay *et al.*, "CNN-based segmentation of medical imaging data," 2017, arXiv:1701.03056.

[25] Y. Zou *et al.*, "Classifying digestive organs in wireless capsule endoscopy images based on deep convolutional neural network," in *Proc. IEEE Int. Conf. Digit. Signal Process.*, 2015, pp. 1274–1278.

[26] Q. Dou *et al.*, "3D deeply supervised network for automatic liver segmentation from CT volumes," 2016, arXiv:1607.00582.

[27] K. H. Cha *et al.*, "Deep-learning-based bladder segmentation in CT urography," in *RSNA Program Book*, 2015, pp. 2–16.

[28] F. Liu *et al.*, "Low-dose liver CT images segmentation and 3D reconstruction," in *Proc. Int. Conf. Electromech. Control Technol. Transp.*, 2015, pp. 309–313.

[29] K. He *et al.*, "Deep residual learning for image recognition," in *Proc. IEEE Conf. Comput. Vision Pattern Recognit.*, 2016, pp. 770–778.

[30] R. K. Srivastava *et al.*, "Training very deep networks," in *Proc. 28th Int. Conf. Neural Inf. Process. Syst.*, 2015, vol. 2, pp. 2377–2385.

[31] W. Cheng and K. Hirakawa, "Towards optimal denoising of image contrast," *IEEE Trans. Image Process.*, vol. 27, no. 7, pp. 3446–3458, Jul. 2018.

[32] L. Xu *et al.*, "Deep convolutional neural network for image deconvolution," in *Proc. 27th Int. Conf. Neural Inf. Process. Syst.*, 2014, vol. 1, pp. 1790–1798.

[33] H. C. Burger *et al.*, "Image denoising: Can plain neural networks compete with BM3D?," in *Proc. IEEE Conf. Comput. Vision Pattern Recognit.*, 2012, pp. 2392–2399.

[34] T. Würfl, *et al.*, "Deep learning computed tomography," in *Proc. Med. Image Comput. and Comput.-Assisted Intervention*, 2016, pp. 432–440.

[35] E. Kang *et al.*, "A deep convolutional neural network using directional wavelets for lowdose X ray CT reconstruction," *Med. Phys.*, vol. 44, no. 10, pp. e360–e375, 2017.

[36] E. Shelhamer *et al.*, "Fully convolutional networks for semantic segmentation," *IEEE Trans. Pattern Anal. Mach. Intell.*, vol. 39, no. 4, pp. 640–651, Apr. 2017.

[37] K. H. Cha *et al.*, "Urinary bladder segmentation in CT urography using deep learning convolutional neural network and level sets," *Med. Phys.*, vol. 43, no. 4, pp. 1882–1896, 2016.

[38] M. Drozdzal *et al.*, "The importance of skip connections in biomedical image segmentation," 2016, arXiv:1608.04117.

[39] O. Ronneberger *et al.*, "U-Net: Convolutional networks for biomedical image segmentation," in *Proc. Med. Image Comput. and Comput.-Assisted Intervention*, 2015, pp. 234–241.

[40] P. F. Christ *et al.*, "Automatic liver and lesion segmentation in CT using cascaded fully convolutional neural networks and 3D conditional random fields," in *Proc. Med. Image Comput. and Comput.-Assisted Intervention*, 2016, pp. 415–423.

[41] F. Lu *et al.*, "Automatic 3D liver location and segmentation via convolutional neural network and graph cut," *Int. J. Comput. Assisted Radiol. Surgery*, vol. 12, no. 2, pp. 171–182, 2017.

[42] P. Hu *et al.*, "Automatic abdominal multi-organ segmentation using deep convolutional neural network and time-implicit level sets," *Int. J. Comput. Assisted Radiol. Surgery*, vol. 12, no. 3, pp. 399–411, 2017.

[43] P. Hu *et al.*, "Automatic 3D liver segmentation based on deep learning and globally optimized surface evolution," *Phys. Med. Biol.*, vol. 61, no. 24, pp. 8676–8698, 2016.

[44] C. Dong *et al.*, "Image super-resolution using deep convolutional networks," *IEEE Trans. Pattern Anal. Mach. Intell.*, vol. 38, no. 2, pp. 295–307, 2016.

[45] F. Agostinelli *et al.*, "Adaptive multi-column deep neural networks with application to robust image denoising," in *Proc. 26th Int. Conf. Neural Inf. Process. Syst.*, 2013, vol. 1, pp. 1493–1501.

[46] Y. Jia *et al.*, "Caffe: Convolutional architecture for fast feature embedding," in *Proc. ACM Int. Conf. Multimedia*, 2014, pp. 675–678.

[47] X. Chen *et al.*, "3D printing and modelling of customized implants and surgical guides for non-human primates," *J. Neurosci. Methods*, vol. 286, pp. 38–55, 2017.

[48] M. Aharon *et al.*, "K-SVD: An algorithm for designing overcomplete dictionaries for sparse representation," *IEEE Trans. Signal Process.*, vol. 54, no. 11, pp. 4311–4322, Nov. 2006.

[49] X. Liu *et al.*, "Automatic organ segmentation for CT scans based on super-pixel and convolutional neural networks," *J. Digit. Imag.*, vol. 31, pp. 1–13, 2018.

[50] R. Gauriau *et al.*, "Multi-organ localization with cascaded global-to-local regression and shape prior," *Med. Image Anal.*, vol. 23, no. 1, pp. 70–83, 2015.

[51] M. G. Linguraru *et al.*, "Statistical 4D graphs for multi-organ abdominal segmentation from multiphase CT," *Med. Image Anal.*, vol. 16, no. 4, pp. 904–914, 2012.

[52] T. Tong *et al.*, "Discriminative dictionary learning for abdominal multi-organ segmentation," *Med. Image Anal.*, vol. 23, no. 1, pp. 92–104, 2015.

[53] T. Okada *et al.*, "Abdominal multi-organ segmentation from CT images using conditional shapelocation and unsupervised intensity priors," *Med. Image Anal.*, vol. 26, no. 1, pp. 1–18, 2015.

[54] R. Wolz *et al.*, "Automated abdominal multi-organ segmentation with subject-specific atlas generation," *IEEE Trans. Med. Imag.*, vol. 32, no. 9, pp. 1723–1730, Sep. 2013.

[55] B. He *et al.*, "Fully automatic multi-organ segmentation based on multi-boost learning and statistical shape model search," in *Proc. VISCERAL Challenge@ISBI*, 2015, pp. 1–5.